Electronic Supplementary Information (ESI) for:

V_2C/VO_2 Nanoribbon Intertwined Nanosheet Congenetic Dual-Heterostructure for Highly Flexible and Robust Lithium-Sulfur Batteries

Mengyao Xu, Tianli Wu, Jing Qi, Dan Zhou and Zhubing Xiao*

Henan Key Laboratory of Photovoltaic Materials, Henan University, Kaifeng, 475004, China.

*Corresponding author

Email: zbxiao@vip.henu.edu.cn

Experimental section

Polysulfide adsorption test

The Li_2S_4 solution was prepared by chemical reaction between sublimed sulfur and Li_2S with a molar ratio of 3:1 in DME solution in an argon-filled glovebox, the solution was stirred at room temperature for 24 h to form a 4 mmol L^{-1} Li_2S_4 stock solution. V_2C, V_2C-140, V_2C-160 and V_2C-180 were added separately to 10 mL of Li_2S_4 solution, followed by mild magnetic stirring for 2 h. The adsorption ability was visually detected by color change of the resultant solution.

Electrochemical measurements

Freestanding sulfur cathode pieces with a diameter of 14 mm were punched out from as-prepared V_2C-160/S or V_2C/S, V_2C-140/S, V_2C-180/S film. The CR2032-type coin-like cells were assembled using self-supporting cathode piece as cathode and lithium foil as anode in Ar-filled glove box. The electrolyte was 1 M Li bis(trifluoromethanesulfonyl) (1,3-dioxolane/1,2-dimethoxyethane, DOL/DME =1:1, v/v) containing 2% $LiNO_3$ and Celgard 2400 film was used as the separator. Galvanostatic charge/discharge measurement was conducted using Land CT2001A battery test system in the voltage window 1.6-2.8 V. Cyclic voltammetry (CV) and electrochemical impedance spectra (EIS) were tested on CHI604E electrochemical workstation. CV was carried out at a scanning rate of 0.1 mV s^{-1} within a voltage window of 1.6-2.8 V and EIS was measured in the frequency range of 100 kHz-0.01 Hz.

Ex situ XRD measurements

Self-supporting electrode materials (V_2C-160/S) were firstly activated at 0.2 C for three cycles. Then, the cycled electrodes were extracted from coin cell in Ar-filled glove box and thoroughly washed by DOL/DME mixture, followed by drying in Ar-filled glove box. The cycled electrodes at different charge/discharge state were sealed before the XRD measurement.

Symmetrical cell assembly and measurements

The electrodes of symmetrical cells were prepared without loading elemental sulfur. The punched flexible electrode disks (14.0 mm) were used as working and counter electrodes. Electrolyte containing 0.4 M Li_2S_6 and 1 M LiTFSI was dissolved in DME, and the same electrolyte was used without Li_2S_6 as the control. The CV measurements of symmetrical cells were performed in the voltage window from -1 to 1 V at a scanning rate of 1 mVs^{-1}.

Galvanostatic intermittent titrations (GITT) measurements

Galvanostatic intermittent titrations (GITT) were carried out on a Land CT3001A battery testing system at 25 °C in the potential window of 1.6-2.8 V. In addition, the cell was charged/discharged at 0.2 C for a constant time of 30 min, followed by a 10 h rest period.

Assembly of flexible Li-S batteries

The Li-S pouch cells were assembled in a glove box by using same cathode materials, electrolyte and separator with coin cells. The dimension of the V_2C-160@S electrode and Li ribbon were cut into 3 cm × 2 cm. The cells were sealed with an aluminum-plastic film. An aluminum tab was connected to the V_2C-160@S electrode, and a nickel tab was connected to the Li ribbon. The E/S ratio was decreased to 4.5 μL mg^{-1} in order to prevent the electrolyte being squeezed out during the folding processes. The cells were rested for 6 h before the electrochemical examinations. The whole electrochemical-examination conditions are the same as that of the coin cells.

Computational method

First-principles calculations were performed using the Vienna *ab initio* simulation package known as the VASP code.[1] The electronic-ion interaction was described by a projector augmented wave method (PAW).[2] The energy cutoff of the plane waves was set to 450 eV. The electron exchange-correlation function was treated using a generalized gradient approximation (GGA) in the form proposed by Perdew, Burke, and Ernzerhof (PBE).[3] Particularly, we used the vdW-DF2 functional to include the physical van der Waals (vdW) interaction in the simulation.[4,5] The Brillouin zone integration was sampled by with 3 × 3 × 1 k-grid mesh for geometry optimization, and 4 × 4 × 1 k-grid mesh for electronic properties calculations to achieve high accuracy. For the bulk VSe_2, both of atomic positions and lattice vectors were fully optimized using the conjugate gradient algorithm until the maximum atomic forces were less than 0.01 eV/Å with an energy precision of 10^{-5} eV.

The binding energies (E_b) of Li_2S_4 on the substrates are defined as:

$$E_b = (E_{Li2S4} + E_{Surf} - E_{Total})$$

where E_{Total} and E_{Surf} are the total energies of V_2C adsorbed with and without Li_2S_4, and E_{Li2S4} is the total energy of the Li_2S_4.

Electron localization function (ELF) is defined as:[6,7]

ELF = $1/(1 + (D/D_h))$, where $D = \frac{1}{2}\sum_i |\nabla \varphi_i|^2 - \frac{1}{8}\frac{|\nabla \rho|^2}{\rho}$ and $D_h = \frac{3}{10}(3\pi^2\rho)^{5/3}$

φ_i represents the Kohn Sham orbitals and $\rho = \sum_i |\varphi_i|^2$ stands for electron charge density. According to the equation, the value of ELF varies from 0 to 1, in which ELF = 1 corresponds to perfect localization of electrons and ELF = 0.5 indicates a uniform electron gas.

Structure characterization

XRD patterns were recorded in the range of 2θ = 5-70° on a desktop X-ray diffractometer (DX2700) with Cu Kα radiation (λ = 1.5406 Å). XPS measurements were performed on a AXIS ULTRA spectrometer (Kratos), using nonmonochromatic Al Kα X-ray as the excitation source and choosing C 1s (284.5 eV) as the reference line. TGA was measured at a heating rate of 10 °C min-1 using a TAQ600 thermo gravimetric analyzer. Nitrogen adsorption/desorption data were recorded at liquid nitrogen temperature (77 K) using a Besorp-Max II (Microtrac BEL) apparatus. Total pore volumes were calculated from the amount adsorbed at a relative pressure (P/P0) of 0.99. The specific surface area was calculated using the Brunauer-Emmett-Teller (BET) equation. SEM images were obtained with a JSM-7001F field-emission scan electron microscope. TEM images were obtained on JEM-2100. UV-vis spectroscopy was performed on a Lambda900 spectrophotometer.

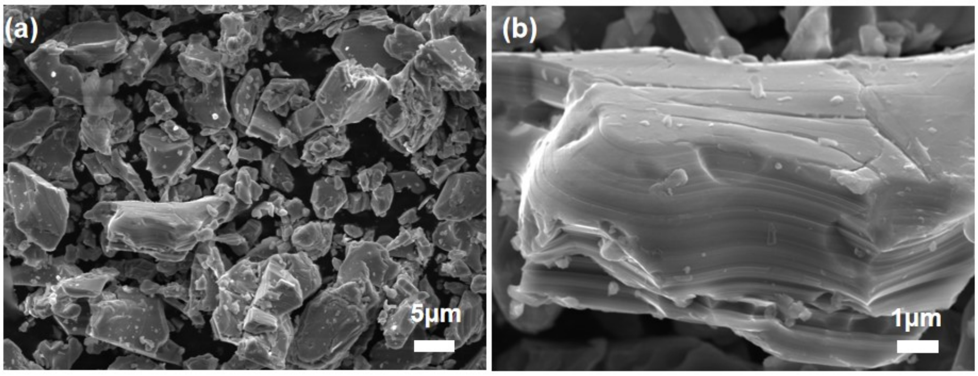

Fig. S1 SEM images of V_2AlC.

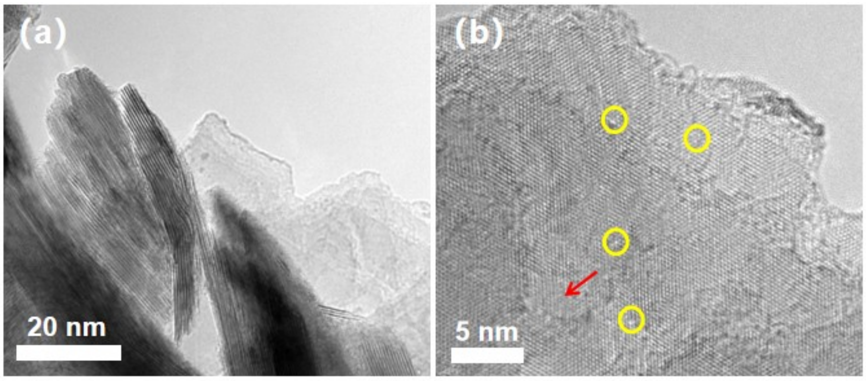

Fig. S2 TEM images of multi-layered V_2C. The red arrows and yellow circles indicate the pore defects.

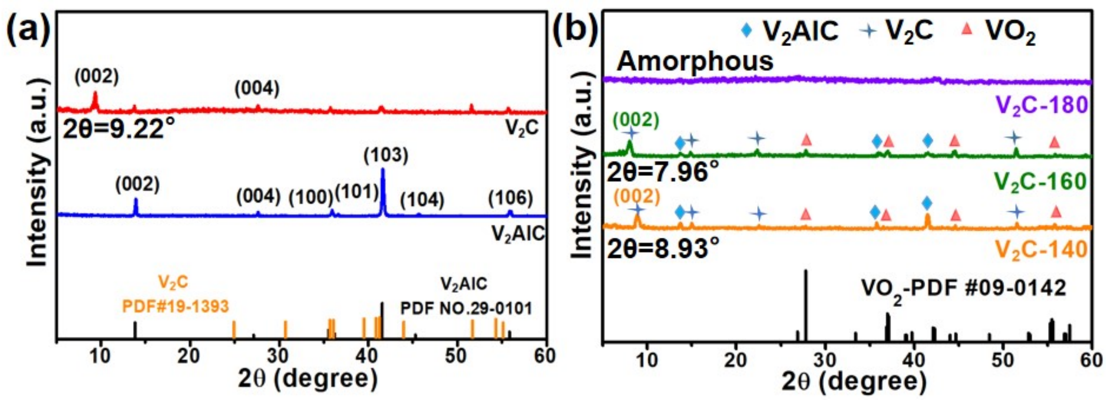

Fig. S3 XRD patterns of (a) commercial V_2AlC, etched V_2C, and (b) hydrothermal-treated V_2C at various temperatures.

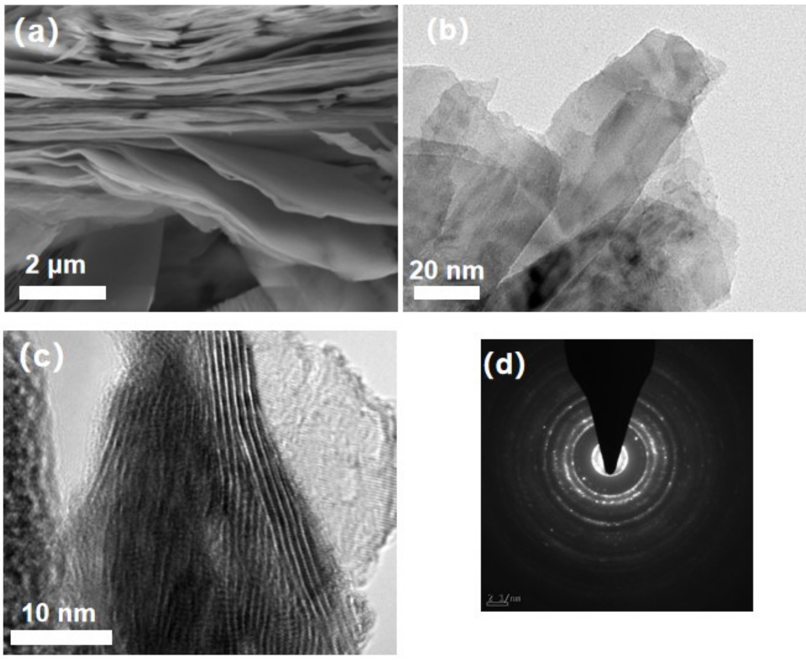

Fig. S4 (a) SEM, (b, c) TEM images and (d) corresponding SAED pattern of the V_2C-160 with hydrothermal treatment for 4 h.

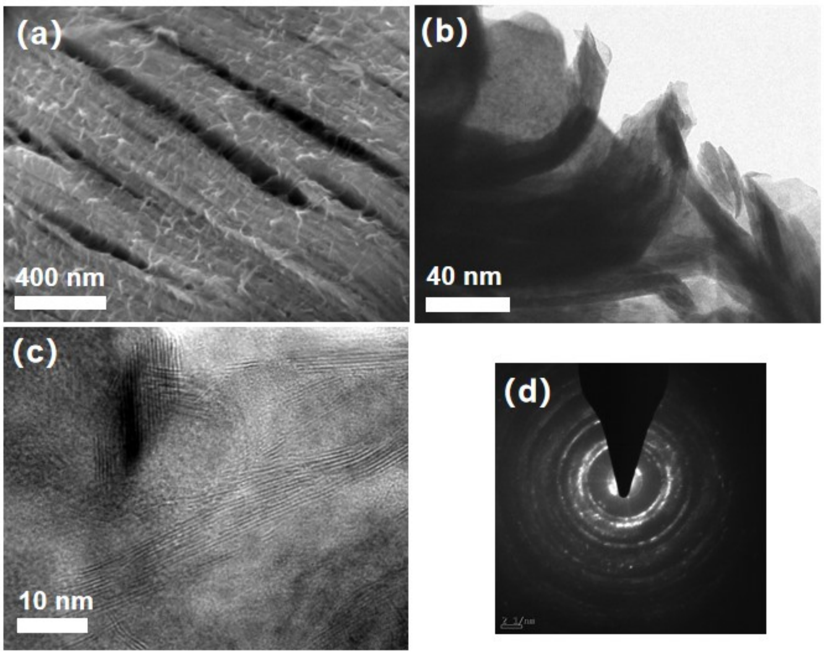

Fig. S5 (a) SEM, (b, c) TEM images and (d) corresponding SAED pattern of the V_2C-160 with hydrothermal treatment for 8 h.

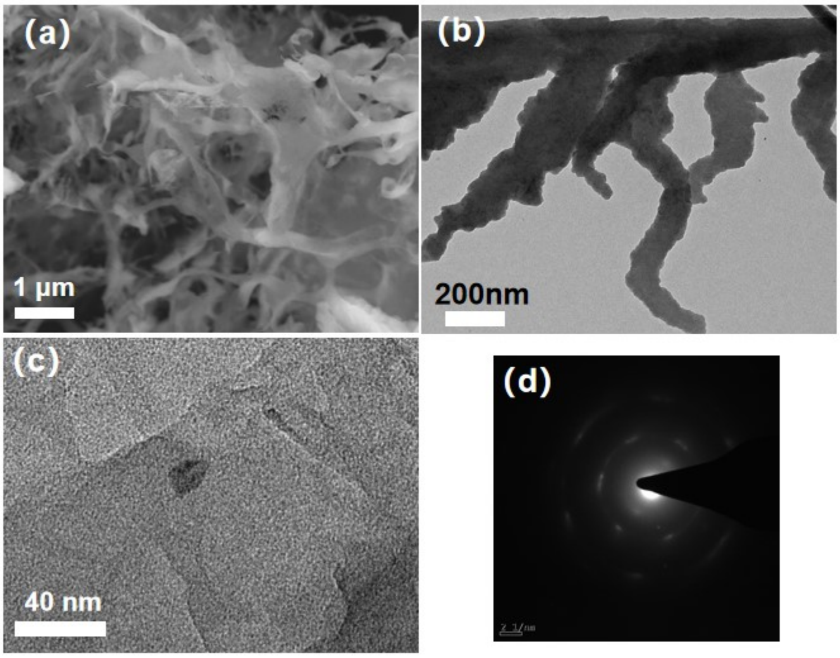

Fig. S6 (a) SEM, (b, c) TEM images and (d) corresponding SAED pattern of the V_2C-160 with hydrothermal treatment for 16 h.

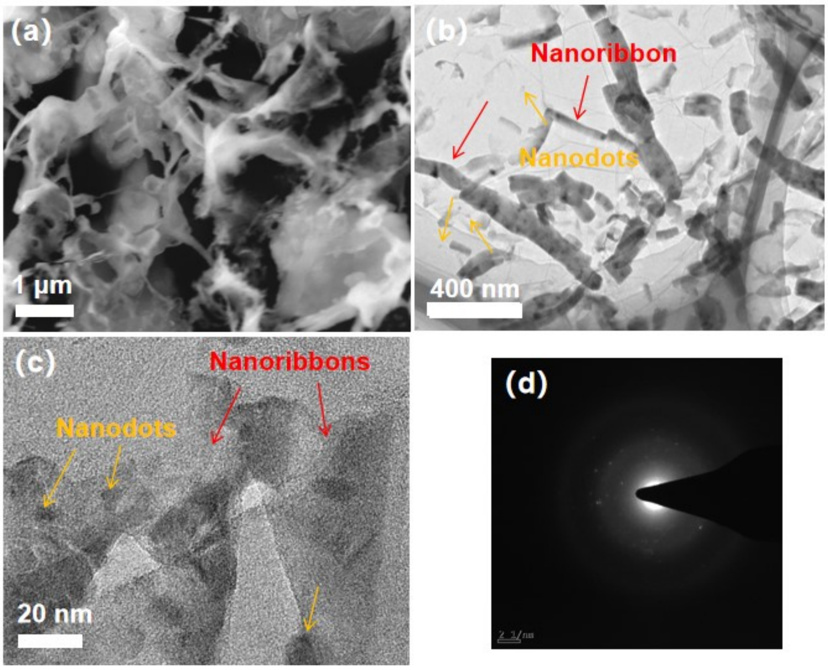

Fig. S7 (a) SEM, (b, c) TEM images and (d) corresponding SAED pattern of the V_2C-160 with hydrothermal treatment for 24 h.

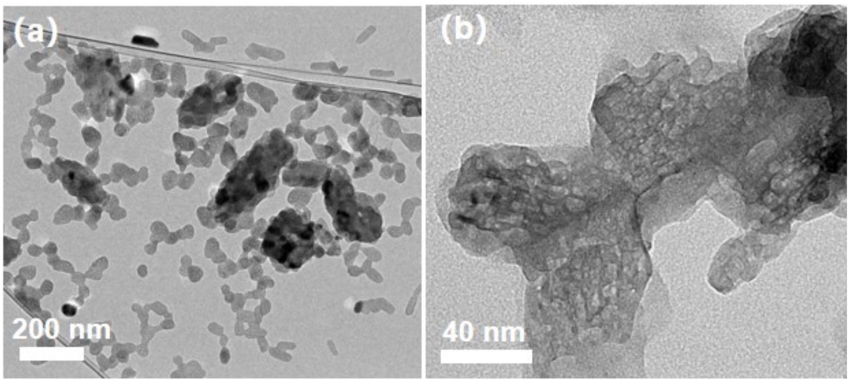

Fig. S8 (a) SEM, (b, c) TEM images and (d) corresponding SAED pattern of the V_2C-160 with hydrothermal treatment for 30 h.

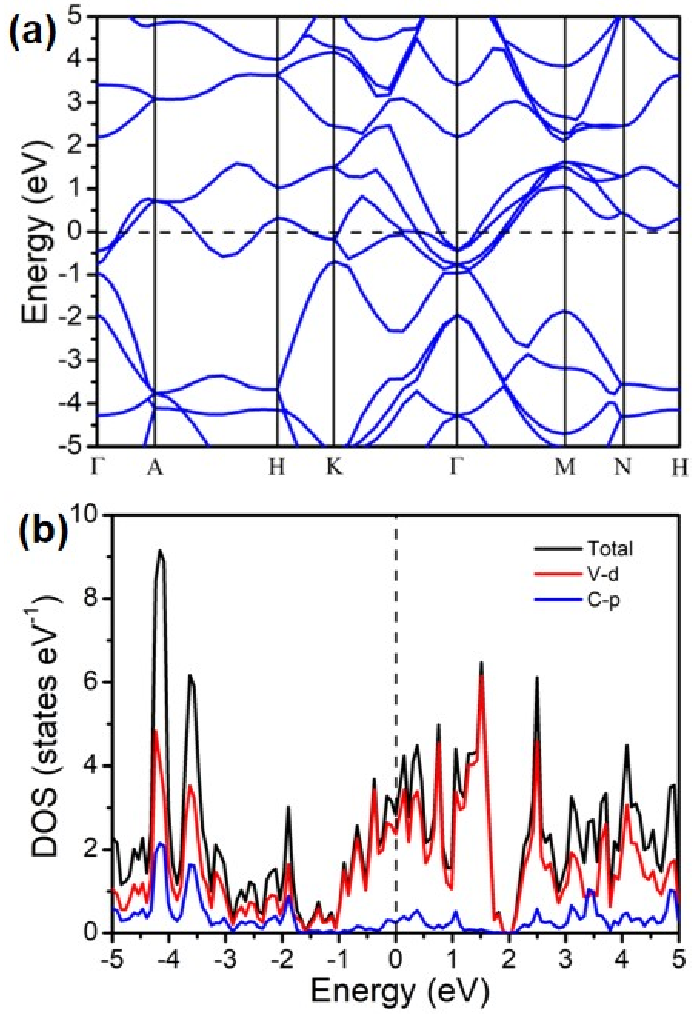

Fig. S9 Calculated (a) band structure and (b) PDOS of V_2C.

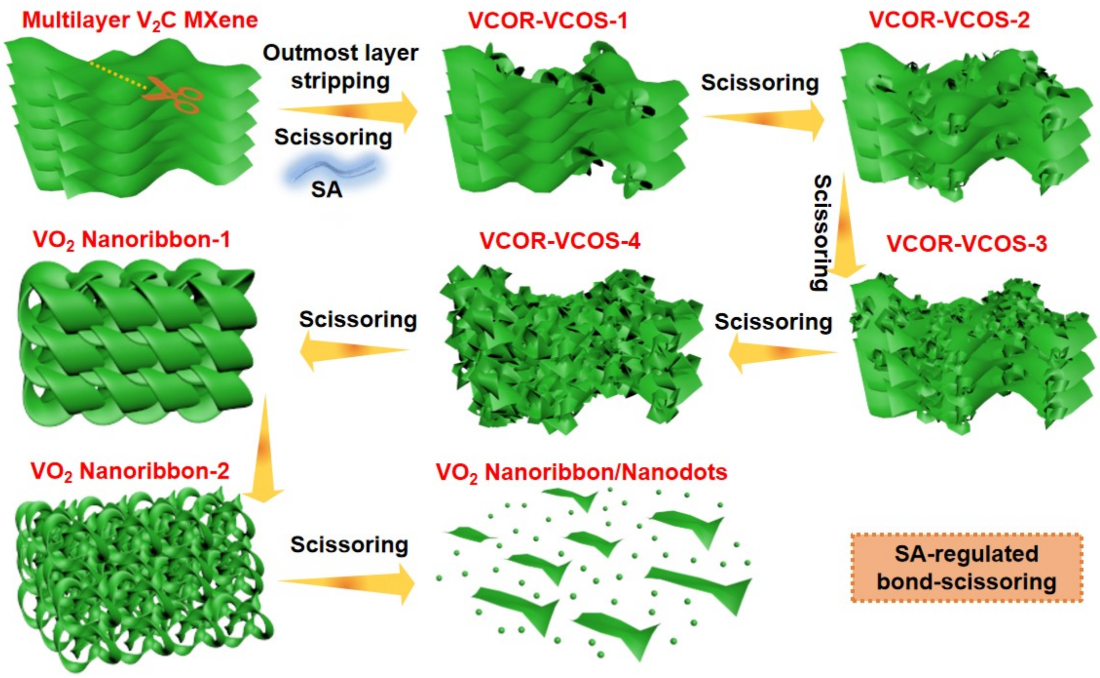

Fig. S10 Scheme for SA-regulated bond-scissoring of the multi-layer V_2C nanosheets.

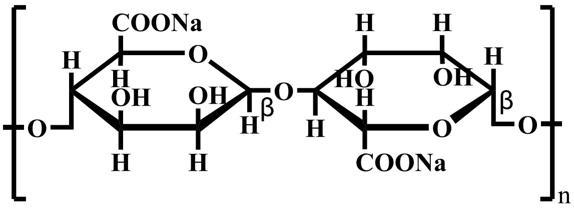

Fig. S11 The molecular structure of SA.

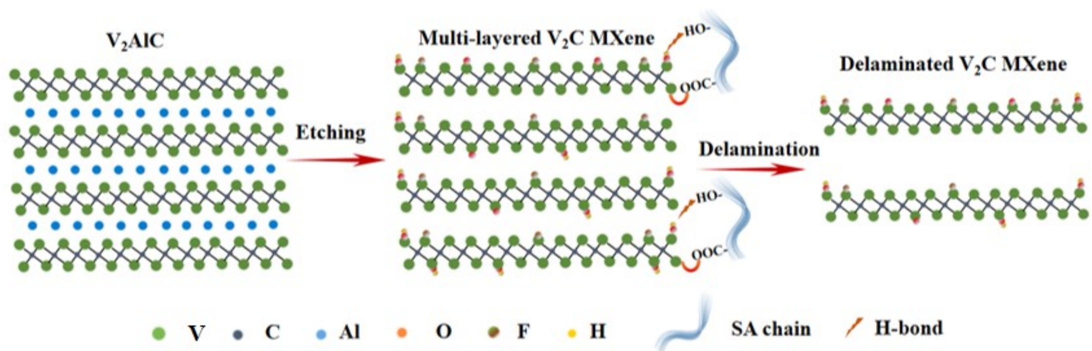

Fig. S12 Scheme for the *in situ* delamination of as-synthesized V_2C nanosheets in the presence of SA.

As can be seen clearly in Fig. S11 and S12, the strong coordination between carboxyl groups of long SA chains and edge V atoms of the V_2C surface as well as extensive hydrogen bonds between V_2C and SA could weaken the V-C bonds and the van der Waals force between the adjacent V_2C nanosheets.

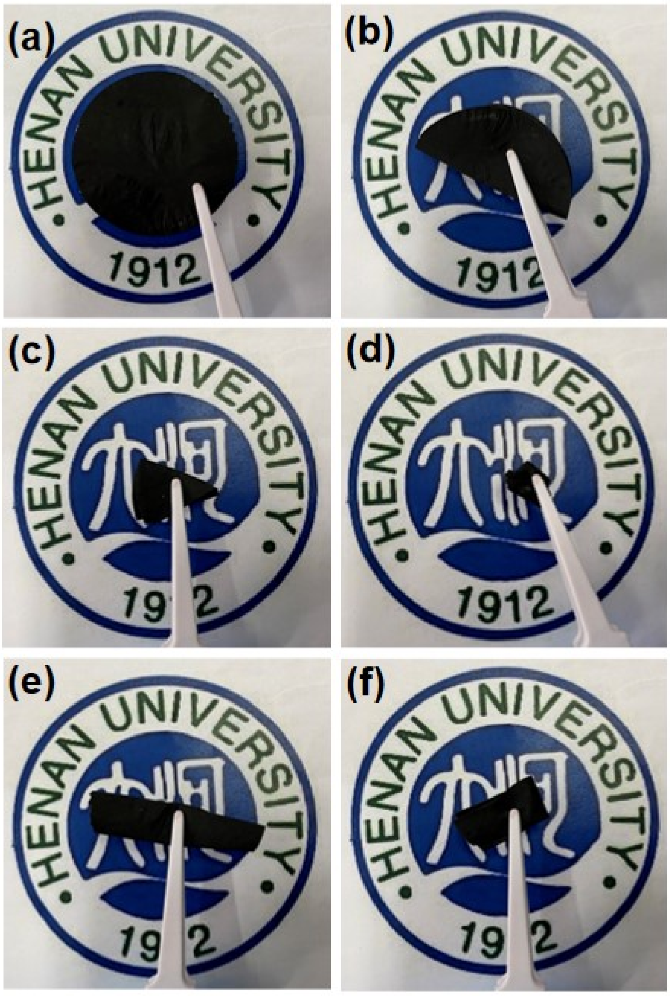

Fig. S13 Digital photos of the self-supporting and flexible V_2C-160 at various bending states.

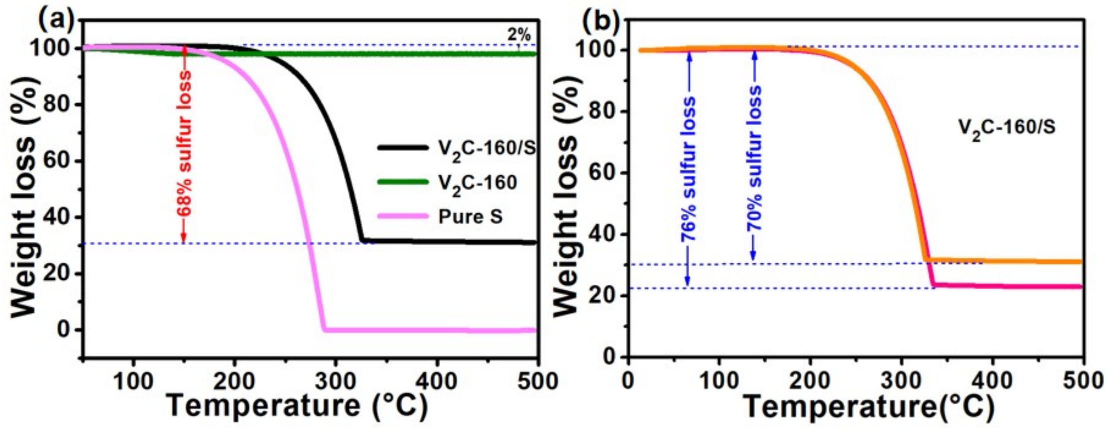

Fig. S14 TGA plots of V_2C-160/S composite with different sulfur content for the electrode with areal sulfur loadings of (a) 1.7 and 2.8 mg cm^{-2} (black line) and (b) 5.6 and 8.6 mg cm^{-2} (orange and pink lines).

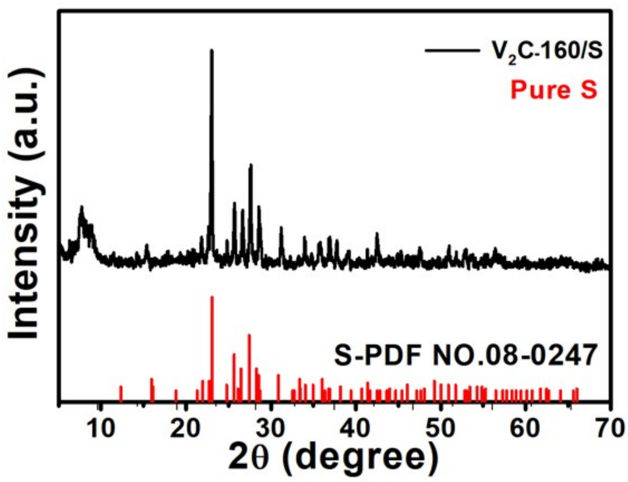

Fig. S15 XRD patterns for V_2C-160/S and pure S.

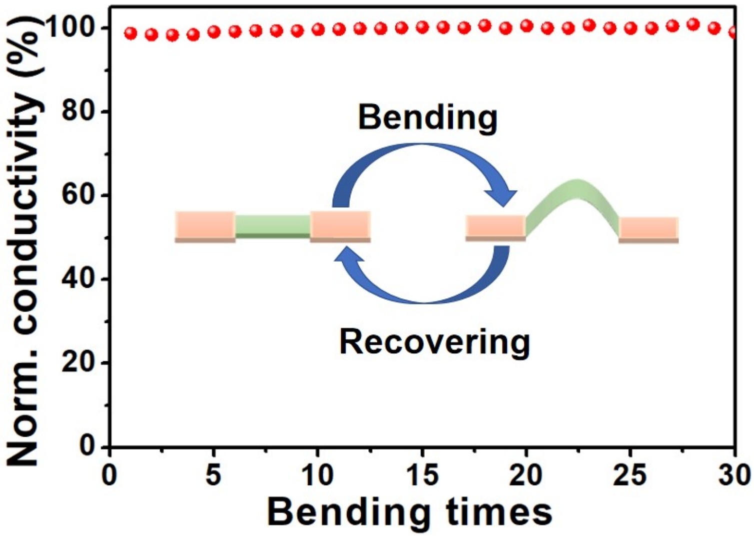

Fig. S16 The normalized conductivity of flexible V_2C-160/S paper versus bending times.

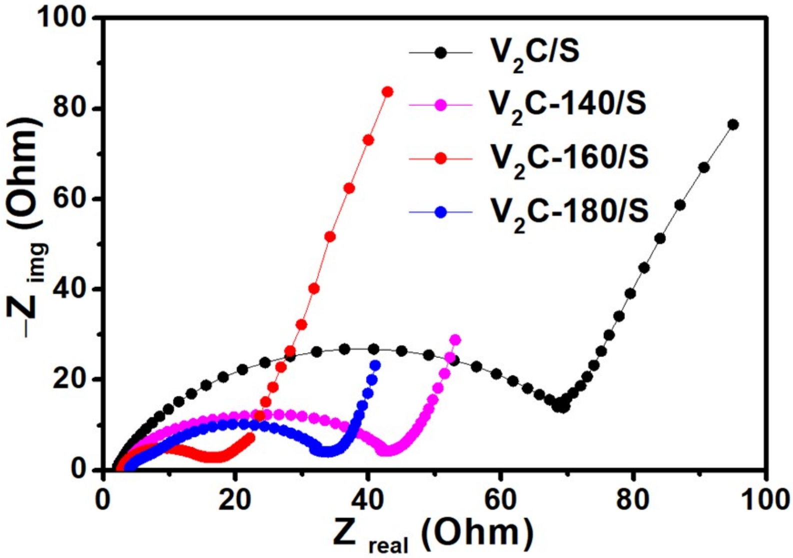

Fig. S17 Nyquist plots for the V_2C/S, V_2C-140/S, V_2C-160/S and V_2C-180/S electrodes.

Table S1. Summary of various hybrid architectures based on 2D MXenes and low-dimensional inorganic nanostructures in terms of morphology, application, and electrochemical performance.

Nanohybrids	Morphology	Application	Performance	Ref
$TiO_2@Ti_3C_2T_x$ s)	Nanoparticles	SIBs a)	≈90 mA h g^{-1} at 0.1 A g^{-1}	[8]
$SnO_2@Ti_3C_2T_x$ s)	Nanowires	LIBs b)	530 mA h g^{-1} at 1 A g^{-1}	[9]
$Nb_2O_5@Nb_4C_3T_x$ s)	Nanoparticles	LIBs	167 mA h g^{-1} at 1 C	[8]
$NiCo_2O_4@Ti_3C_2T_x$ s)	Nanoparticles	LIBs	≈410 mA h g^{-1} at 5C	[10]
$NiCo_2O_4@Ti_3C_2T_x$ s)	Nanoflakes	LIBs	≈1200 mA h g^{-1} at 1 C	[10]
$Co_3O_4@Ti_3C_2T_x$ s)	Nanoflakes	LIBs	≈650 mA h g^{-1} at 1 C	[10]
$Na_{0.23}TiO_2@Ti_3C_2T_x$ s)	Nanobelts	LIBs	178 mA h g^{-1} at 5 A g^{-1}	[11]
$Na_{0.23}TiO_2@Ti_3C_2T_x$ s)	Nanobelts	SIBs	56 mAh g^{-1} at 2 A g^{-1}	[11]
$Fe_3O_4@Ti_3C_2T_x$ s)	Nanoparticles	LIBs	2038 mA h cm^{-3} at 1 C	[12]
$SnS@Ti_3C_2T_x$ s)	Nanoparticles	SIBs	256 mA h g^{-1} at 1 A g^{-1}	[13]
$BP@Ti_3C_2T_x$ s)	Quantum dots	LIBs	520 mA h g^{-1} at 1 A g^{-1}	[14]
GRO@S f)	Nanosheets	LSB c)	1107 mA h g^{-1} at 0.2 C	[15]
1T-2H MoS_2-$C@Ti_3C_2T_x$ s)	Nanosheets	LSB	677.2 mA h g^{-1} at 2 C	[16]
Meso-$C@Ti_3C_2T_x$ s)	Nanosheets	LSB	727.8mA h g^{-1} at 2 C	[17]
PEI–$CNT@Ti_3C_2T_x$ s)	Nanosheets	LSB	≈950 mA h g^{-1} at 2.5 C	[18]
$CNT@Nb_2CT_x$ f)	Paper	LIBs	≈370 mA h g^{-1} at 2.5 C	[19]
VO_2(p)$@V_2CT_x$ s)	Nanorods	LSB	756 mA h g^{-1} at 2C	[20]
$V_2O_5@V_2CT_x$ s)	Nanotube	LSB	1086mA h g^{-1} at 0.2 C	[21]
TS-Ti_3C_2/CNT s)	Microsphere	LSB	1225mA h g^{-1} at 0.2 C	[22]
$Ti_3C_2T_x$ paper f)	Nanosheets	LSB	1270mA h g^{-1} at 0.5 C	[23]
PSU-Celgard separators f)	Nanosheets	LSB	1112.8mA h g^{-1} at 0.5 C	[24]
rGO/CNT f)	Paper	LSB	1051mA h g^{-1} at 0.5 C	[25]
Co@NCNP/NCNT f)	Microsphere	LSB	703mA h g^{-1} at 0.15 C	[26]
CNT/PPy@CS f)	Paper	LSB	1124 mA h g^{-1} at 0.1 A g^{-1}	[27]
g-C_3N_4@CC f)	Carbon fibers	LSB	937.4mA h g^{-1} at 0.5 C	[28]
NCF/CNT/PEDOT@S f)	Nanoarrays	LSB	1167mA h g^{-1} at 0.2 C	[29]
MoS_2@CMT f)	Microtubes	LSB	1162mA h g^{-1} at 0.5 C	[30]
PS/W_2C-CNFs f)	Nanoparticles	LSB	1200mA h g^{-1} at 0.2 C	[31]
TiO_2/C f)	Nanoparticles	LSB	1102mA h g^{-1} at 0.5 C	[32]
PCNFs-2 f)	Nanofibers	LSB	1028mA h g^{-1} at 0.2 C	[33]
V_2CT_x/VO_2 f)	Nanoribbon	LSB	1254mA h g^{-1} at 0.2 C	This Work

a) Sodium-ion batteries; b) Lithium-ion batteries; c) Li-S batteries. s) slurry-coating cathode; f) flexible cathode.

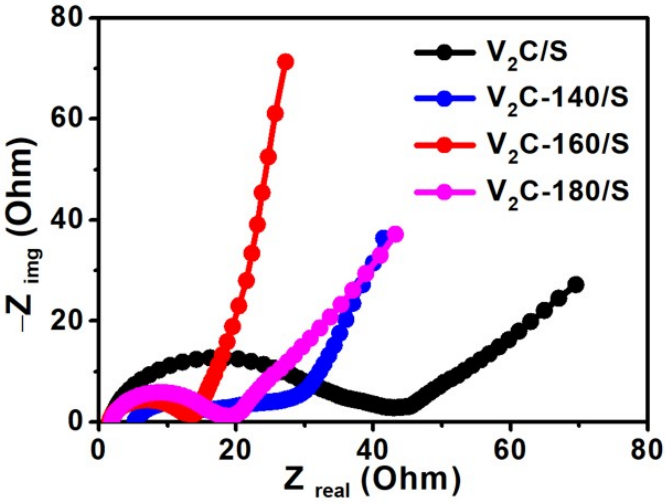

Fig. S18 Nyquist plots for the V_2C/S, V_2C-140/S, V_2C-160/S and V_2C-180/S electrodes after 100 cycles at 0.5 C.

As shown in Fig. S17† and S18†, a much depressed quasi-semicircle in the high-frequency region and a more inclined line in the low-frequency region are observed in the V_2C-160/S electrode, indicative of rapid electron/ion-transfer kinetics.

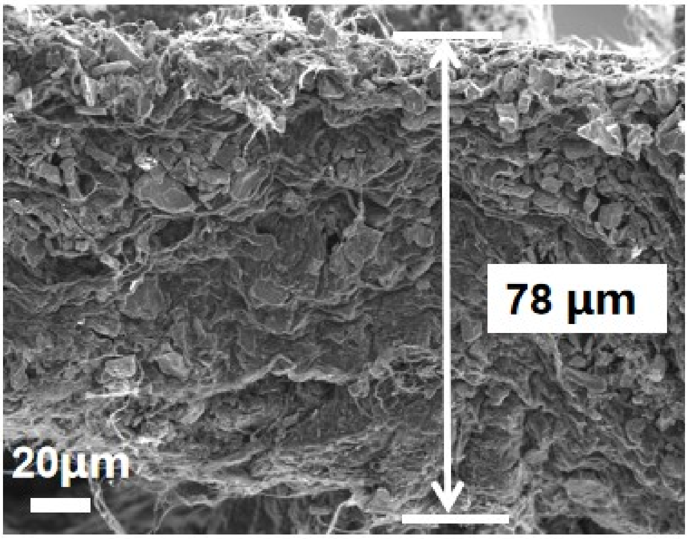

Fig. S19 Cross-section SEM image of the self-supporting V_2C-160/S cathode with areal sulfur loading of 8.6 mg cm^{-2}. The average thickness of 78 um was obtained after testing five cathode pieces.

Table S2. Comparison of sulfur loading, mass capacity based on sulfur mass alone, gravimetric/areal/volumetric capacities. The data are collected from recent reports with areal sulfur loading between 5-15 mg cm^{-2}.

Cathode materials	Sulfur loading [mg cm^{-2}]	Gravimetric capacity [mAh g^{-1}]	Areal capacity [mAh cm^{-2}]	Volumetric capacity [mAh cm^{-3}]	Ref.
Layer-by-layer sulfur cathode[b)]	11.4	560	6.4	113, 0.2 C	[34]
Pie-like sulfur cathode[b)]	10.8	536	5.8	397, 0.2 C	[35]
Li_2S_6 loaded in CNF@MnO_2[b)]	7.2	575	4.1	262, 0.2 C	[36]
MWCNT@S[b)]	9.28	840	7.8	577, 0.2 C	[37]
G@HMCN/S-G[b)]	10.0	918	9.2	1350, 0.1 C	[38]
CoP@G/CC-S[b)]	10.83	813	8.81	Not given, 0.05 C	[39]
3DP-LaB_6/SP@S[b)]	9.3	833	7.75	262.7, 0.05 C	[40]
GC-TiO@CHF/S[a)]	5	700	3.5	630, 0.2 C	[41]
FLPT-S[a)]	10.5	564	5.93	1185, 0.033 C	[42]
TC-100/S[a)]	9.2	698	6.42	1235, 0.05 C	[43]
IBGM-S[b)]	5.6	928	5.2	653	[44]
SACNT@SNC@S[b)]	7	896.5	6.3	Not given, 0.5 C	[45]

S@HKUST[a)]	11.33	658	7.45	820, 0.1 C	[46]
RGO@S films[b)]	5.8	1238	7.2	Not given, 0.1 C	[47]
VCOR-VCOS/S[b)]	**8.6**	**954**	**8.2**	**1192, 0.2 C**	**This work**

a) non-flexible cathode, b) flexible cathode.

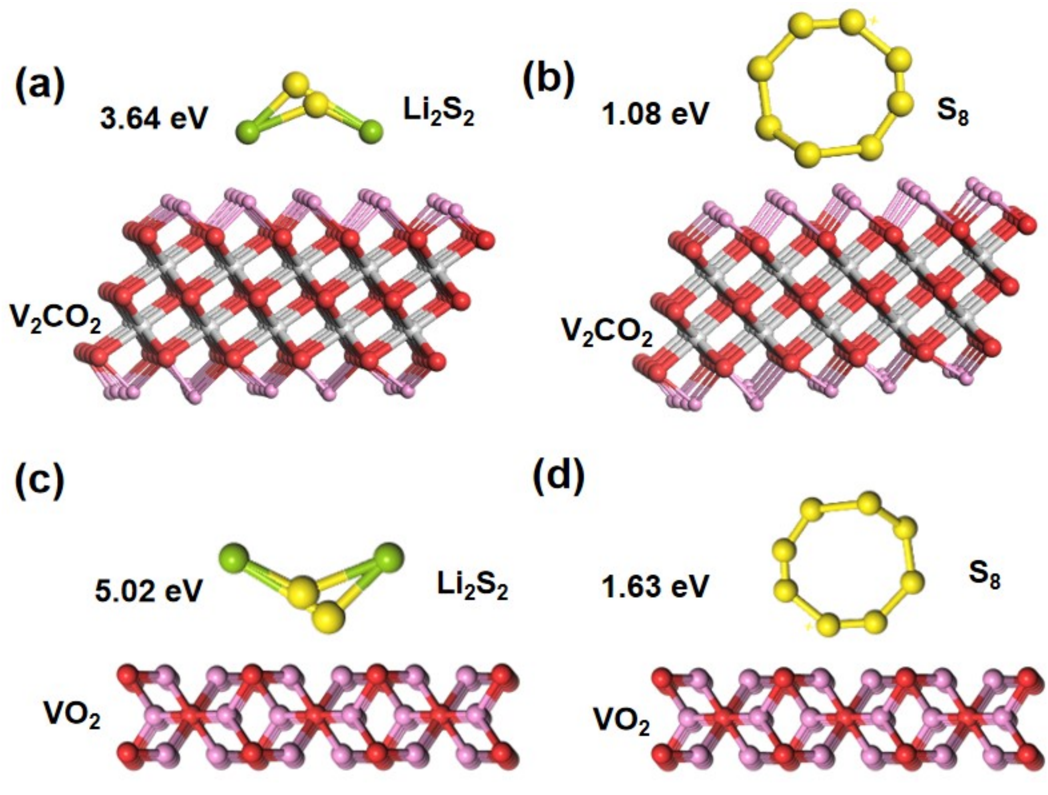

Fig. S20 Binding energy values and corresponding optimized geometry of Li_2S_2 and S_8 adsorbed on the surfaces of V_2CO_2 (a-b) and VO_2 (c-d).

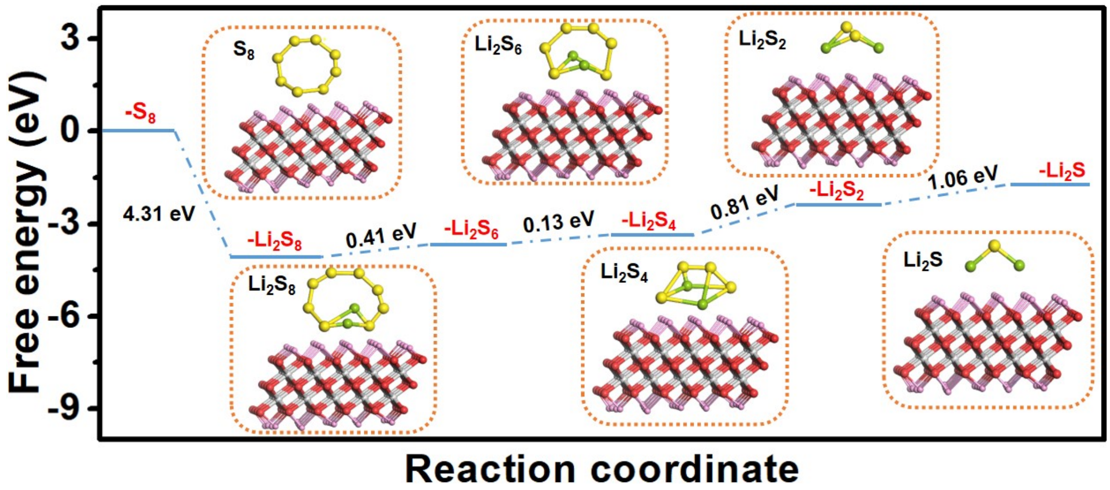

Fig. S21 Energy profiles for the reduction of LiPS on V_2CO_2, The insets in (Figure S20) are the optimized adsorption conformations of sulfur-related species on V_2CO_2.

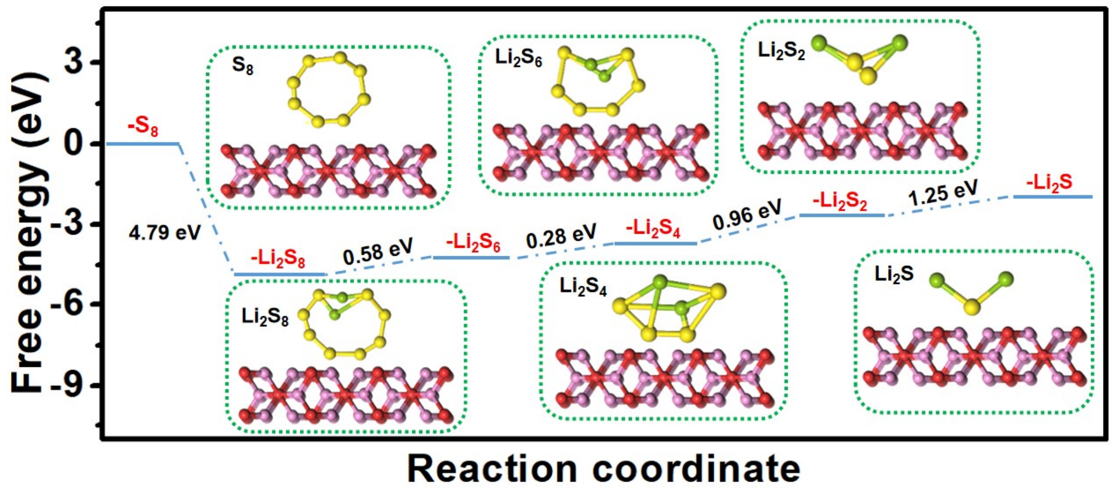

Fig. S22 Energy profiles for the reduction of LiPS on VO_2. The insets in (Figure S21) are the optimized adsorption conformations of sulfur-related species on VO_2.

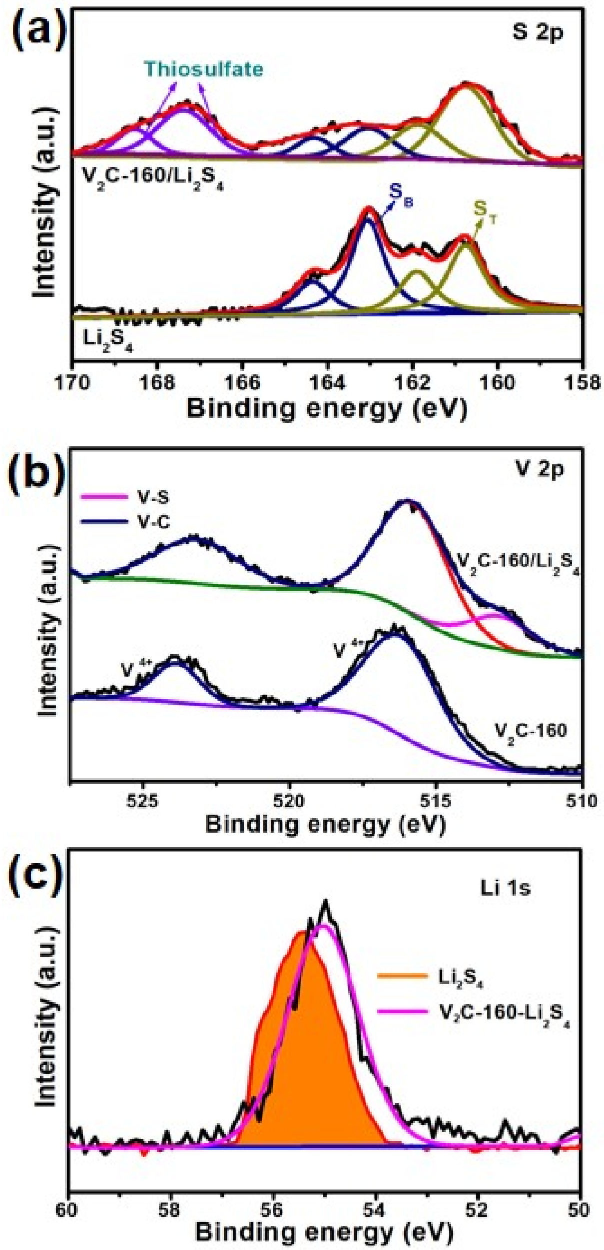

Fig. S23 (a) S 2p XPS spectra of Li_2S_4 and V_2C-160/Li_2S_4 composite, (b) V 2p XPS spectra of V_2C-160 and V_2C-160/Li_2S_4 composite, and (c) Li 1s XPS spectra of Li_2S_4 and V_2C-160/Li_2S_4 composite.

Fig. S24 Photographs of the anodes, separators and cathode pieces of the V_2C/S, V_2C-140/S, V_2C-160/S and V_2C-180/S cells (from left to right) after 500 cycles at 0.5 C.

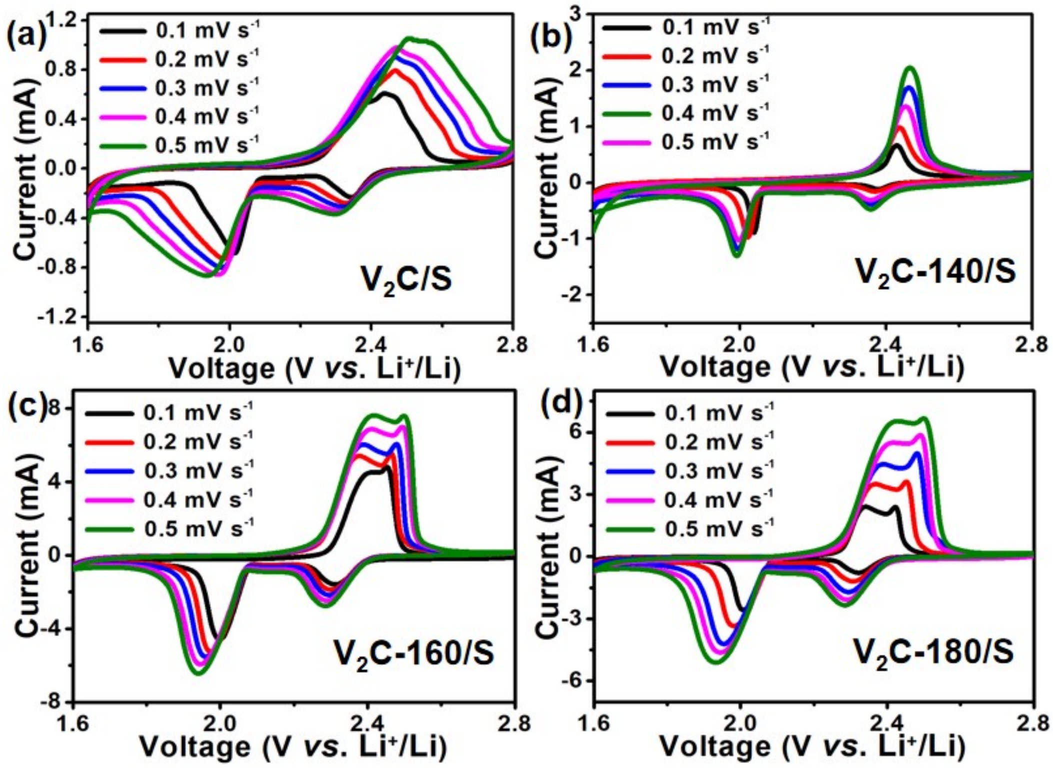

Fig. S25 CV curves of (a) V_2C/S, (b) V_2C-140/S, (c) V_2C-160/S and (d) V_2C-180/S electrodes at different scan rates from 0.1 to 0.5 mV s^{-1}.

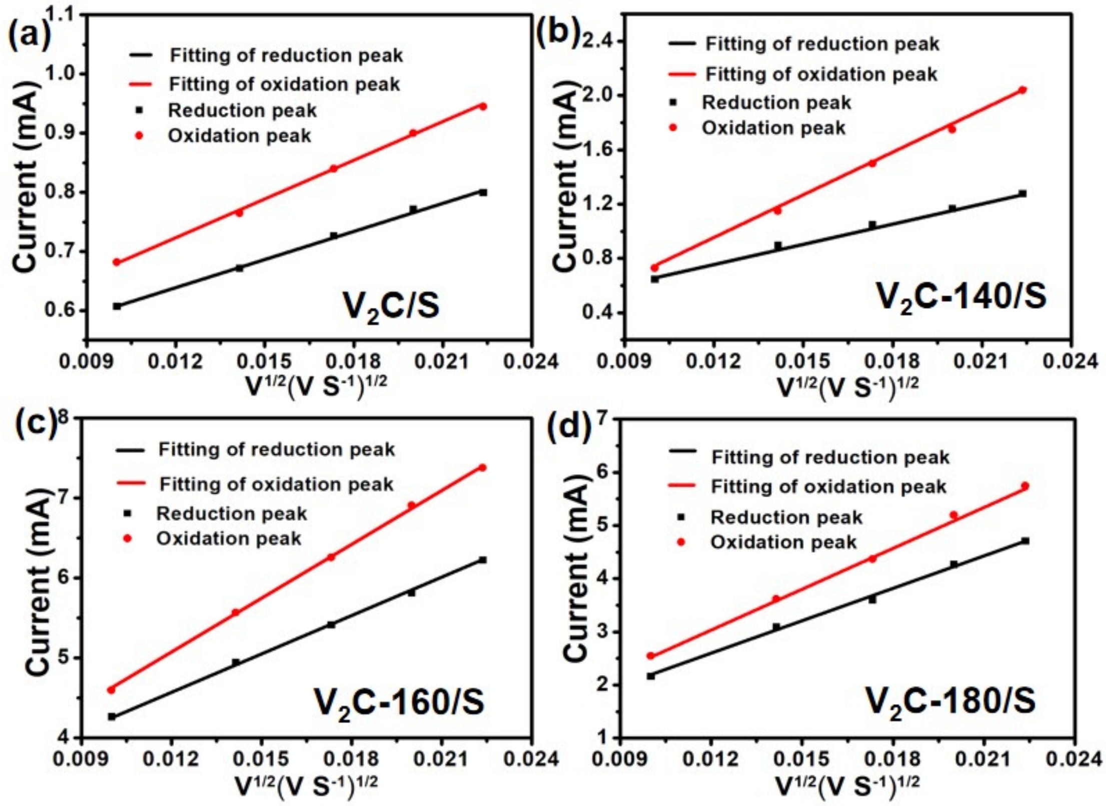

Fig. S26 The plots of CV peak currents *vs.* square root of scan rates for (a) V_2C/S, (b) V_2C-140/S, (c) V_2C-160/S and (d) V_2C-180/S electrodes.

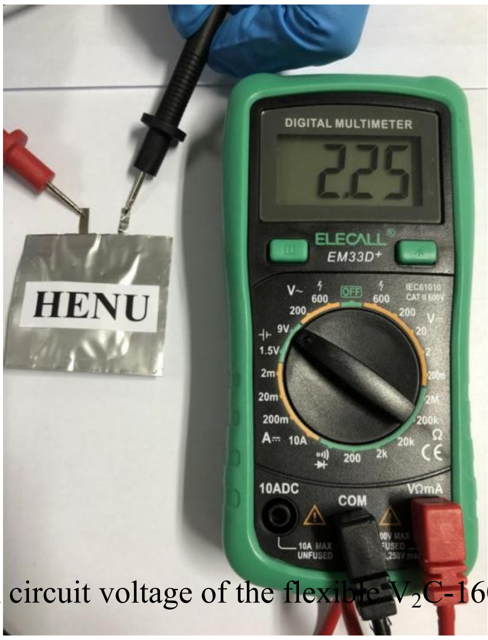

Fig. S27 Open circuit voltage of the flexible V_2C-160/S pouch cell.

References

[S1] G. Kresse and J. Furthmuller, *Phys. Rev. B.*, 1996, **54**, 11169.

[S2] J. P. Perdew, J. A. Chevary, S. H. Vosko, K. A. Jackson, M. R. Pederson, D. J. Singh and C. Fiolhais, *Phys. Rev. B.*, 1992, **46**, 6671.

[S3] V. I. Anisimov, J. Zaanen and O. K. Andersen, *Phys. Rev. B.*, 1991, **44**, 943.

[S4] J. Klimeš, D. R. Bowler and A. J. Michaelides, *Phys. Rev. B.*, 2011, **83**, 195131.

[S5] K. Lee, É. D. Murray, L. Kong, B. I. Lundqvist and D. C. Langreth, *Phys. Rev. B.*, 2010, **82**, 081101.

[S6] B. Silvi and A. Savin, *Nature*, 1994, **371**, 683-686.

[S7] A. Savin, R. Nesper, S. Wengert and T. E. Fässler, *Angew. Chem. Int. Ed.*, 1997, **36**, 1808-1832.

[S8] C. Zhang, S. J. Kim, M. Ghidiu, M. Q. Zhao, M. W. Barsoum, V. Nicolosi and Y. Gogotsi, *Adv. Funct. Mater.*, 2016, **26**, 4143-4151.

[S9] Y. T. Liu, P. Zhang, N. Sun, B. Anasori, Q. Z. Zhu, H. Liu, Y. Gogotsi and B. Xu, *Adv. Mater.*, 2018, **30**, 1707334.

[S10] M. Zhao, M. Torelli, C. E. Ren, M. Ghidiu, Z. Ling, B. Anasori, M. W. Barsoum and Y. Gogotsi, *Nano Energy*, 2016, **30**, 603-613.

[S11] J. M. Huang, R. J. Meng, L. H. Zu, Z. J. Wang, N. Feng, Z. Y. Yang, Y. Yu and J. H. Yang, *Nano Energy*, 2018, **46**, 20-28.

[S12] Y. Wang, Y. Li, Z. Qiu, X. Wu, P. Zhou, T. Zhou, J. Zhao, Z. Miao, J. Zhou and S. Zhuo, *J. Mater. Chem. A.*, 2018, **6**, 11189-11197.

[S13] Y. Zhang, B. Guo, L. Hu, Q. Xu, Y. Li, D. Liu and M. Xu, *J. Alloys Compd.*, 2018, **732**, 448-453.

[S14] R. J. Meng, J. M. Huang, Y. T. Feng, L. H. Zu, C. X. Peng, L. R. Zheng, L. Zheng, Z. B. Chen, G. L. Liu, B. J. Chen, Y. L. Mi and J. H. Yang, *Adv. Energy Mater*., 2018, **8**, 1801514.

[S15] Z. B. Xiao, Z. L. Li, P. Y. Li, X. P. Meng and R. H. Wang, *Nano Energy*, 2020, **70**, 104522.

[S16] Y. L. Zhang, Z. J. Mu, C. Yang, Z. K. Xu, S. Zhang, X. Y. Zhang, Y. J. Li, J. P. Lai, Z. H. Sun, Y. Yang, Y. G. Chao, C. J. Li, X. X. Ge, W. X. Yang and S. J. Guo, *Adv. Funct. Mater*., 2018, **28**, 1707578.

[S17] W. Z. Bao, D. W. Su, W. X. Zhang, X. Guo and G. X. Wang, *Adv. Funct. Mater*., 2016, **6**, 8746.

[S18] D. Guo, F. W. Ming, H. Su, Y. Q. Wu, W. Wahyudi, M. L. Li, M. N. Hedhili, G. Sheng, L. J. Li, H. Alshareef, Y. X. Li and Z. P. Lai, *Nano Energy*, 2019, **61**, 478-485.

[S19] O. Mashtalir, M. R. Lukatskaya, M. Q. Zhao, M. W. Barsoum and Y. Gogotsi, *Adv. Mater*., 2015, **27**, 3501.

[S20] Z. G. Wang, K. Yu, Y. Feng, R. J. Qi, J. Ren and Z. Q. Zhu, *ACS Appl. Mater. Interfaces*., 2019, **11**, 44282-44292.

[S21] Z. G. Wang, K. Yu, S. J. Gong, E. Du and Z. Q. Zhu, *Nanoscale*, 2020, **12**, 18950-18964.

[S22] X. Wang, D. Luo, J. Y. Wang, Z. H. Sun, G. L. Cui, Y. X. Chen, T. Wang, L. R. Zheng, Y. Zhao, L. L. Shui, G. F. Zhou, K. Kempa, Y. G. Zhang and Z. W. Chen, *Angew. Chem. Int. Ed*., 2020, **59**, 2-10.

[S23] H. Tang, W. L. Li, L. M. Pan, K. J. Tu, F. Du, T. Qiu, J. Yang, C. P. Cullen, N. McEvoy and C. F. Zhang, *Adv. Funct. Mater*., 2019, **29**, 1901907.

[S24] B. Z. Yu, Y. Fan, S. Mateti, D. G. Kim, C. Zhao, S. G. Lu, X. Liu, Q. Z. Rong, T. Tao, K. K. Tanwar, X. Tan, S. C. Smith and Y. I. Chen, *ACS Nano*, 2021, **15**, 1358-1369.

[S25] X. Fang, W. Weng, J. Ren and H. S. Peng, *Adv. Mater*., 2016, **28**, 491-496.

[S26] W. Yan, J. Wei, T. Chen, L. Duan, L. Wang, X. L. Xue, R. P. Chen, W. H. Kong, H. N. Lin, C. H. Li and Z. Jin, *Nano Energy,* 2021, **80**, 105510.

[S27] X. W. Fu, F. Dunne, M. Chen and W. H. Zhong, *Nanoscale*, 2020, **12**, 5483-5493.

[S28] H. H. Li, H. Q. Chen, Y. Xue, Y. T. Zhang, M. J. Zhang, W. Q. Yu, G. Y. Bai, K. L. Zhuo and Y. P. Zheng, *Adv. Energy Mater*., 2020, **10**, 2001683.

[S29] M. Zhang, K. Amin, M. Cheng, H. X. Yuan, L. J. Mao, W. Yan and Z. X. Wei, *Nanoscale*, 2018, **10**, 21790.

[S30] J. Y. Yang, L. H. Yu, B. B. Zheng, N. R. Li, J. Y. Xi and X. P. Qiu, *Adv. Sci*., 2020, **7**, 1903260.

[S31] M. J. Yao, R. Wang, Z. F. Zhao, Y. Liu, Z. Q. Niu and J. Chen, *ACS Nano*, 2018, **12**, 12503-12511.

[S32] F. Zhou, Z. Li, X. Luo, T. Wu, B. Jiang, L. L. Lu, H. B. Yao, M. Antonietti, and S. H. Yu, *Nano Lett*., 2018, **18**, 1035-1043.

[S33] F. Y. Hu, H. Peng, T. P. Zhang, W. L. Shao, S. Y. Liu, J. Y. Wang, C. H. Wang and X. G. Jian, *J. Energy Chem*., 2021, **58**, 115-123.

[S34] L. Qie and A. Manthiram, *Adv. Mater*., 2015, **27**, 1694-1700.

[S35] Z. Li, J. Zhang, Y. Chen, J. Li and X. W. Lou, *Nat. Commun*., 2015, **6**, 8850.

[S36] H. Xu, L. Qie and A. Manthiram, *Nano Energy*, 2016, **26**, 224-232.

[S37] H. Kim, Y. H. Lee, S. J. Cho, J. G. Gwon, H. J. Cho, M. Jang, S. Y. Lee and S. Y. Lee, *Energy Environ. Sci*., 2019, **12**, 177-186.

[S38] F. Pei, L. L. Lin, D. H. Ou, Z. M. Zheng, S. G. Mo, X. L. Fang and N. F. Zheng, *Nat. Commun*., 2017, **8**, 482.

[S39] J. Jin, W. L. Cai, J. S. Cai, Y. L. Shao, Y. Z. Song, Z. Xia Q. Zhang and J. Y. Sun, *J. Mater. Chem. A*., 2020, 8, 3027-3034.

[S40] J. S. Cai, Z. D. Fan, J. Jin, Z. X. Shi, S. X. Dou, J. Y. Sun and Z. F. Liu, *Nano Energy*, 2020, **75**, 104970.

[S41] Z. Li, B. Y. Guan, J. Zhang and X. W. Lou, *Joule*, 2017, **1**, 576-587.

[S42] Z. B. Xiao, Z. L. Li, P. Y. Li, X. P. Meng and R. H. Wang, *ACS Nano*, 2019, **13**, 3404-3412.

[S43] Z. B. Xiao, Z. L. Li, P. Y. Li, X. P. Meng and R. H. Wang, *ACS Nano*, 2019, **13**, 3608-3617.

[S44] H. Li, Y. Tao, C. Zhang, D. H. Liu, J. Y. Luo, W. C. Fan, Y. Xu, Y. Z. Li, C. H. You, Z. Z. Pan, M. C. Ye, Z. Y. Chen, Z. Dong, D. W. Wang, F. Y. Kang, J. Lu and Q. H. Yang, *Adv. Energy Mater*., 2018, **8**, 1703438.

[S45] L. J. Jia, J. Wang, Z. J. Chen, Y. P. Su, W. Zhao, D. T. Wang, Y. Wei, K. L. Jiang, J. P. Wang, Y. Wu, J. Li, W. H. Duan, S. S. Fan and Y. G. Zhang, *Nano Res*., 2019, **12**, 1105-1113.

[S46] Q. Pang, X. Liang, C. Y. Kwok, J. Kulisch and L. F. Nazar, *Adv. Energy Mater.*, 2017, **7**, 1601630.

[S47] Y. Liu, M. J. Yao, L. L. Zhang and Z. Q. Niu, *J. Energy Chem.*, 2019, **38**, 199.